Self-propelled capsule endoscopy for small-bowel examination: Proof-of-concept and model verification

Bingyong Guo [a], Yang Liu [a,*], Rauf Birler [a], Shyam Prasad [b]

[a] *College of Engineering, Mathematics, and Physical Sciences, University of Exeter, North Park Road, Exeter EX4 4QF, UK*
[b] *Royal Devon and Exeter NHS Foundation Trust, Barrack Road, Exeter EX2 5DW, UK*

ARTICLE INFO

ABSTRACT

This paper reports the experimental study of a vibro-impact self-propulsion technique applying for small-bowel endoscopy by using a mesoscale capsule prototype, which is 56.9 mm in length and 19.4 mm in diameter. Based on nonsmooth multibody dynamics, a mathematical model is developed for studying the dynamical characteristics of the prototype. Numerical and experimental results are compared to validate the efficacy of the proposed model as well as the feasibility of the technique under various frictional environments. By using the model, we can reveal some hidden dynamics of the prototype and optimise its progression speed and energy efficiency. Based on our calculations, by adopting this technique, the standard-sized capsule, which is 26 mm in length and 11 mm in diameter, can achieve the maximum average speeds of 8.49 mm/s for forward progression and 4.9 mm/s for backward progression, offering the potential for a 'live' and controllable small-bowel examination.

1. Introduction

Developing small-size robots for examining the surface lining of the small intestine [1–7] is a challenging task, particularly for the design of propulsion mechanisms, see e.g. [8,9]. The complexity in design is the hurdle restricting the miniaturisation of the propulsion mechanisms into the dimension of the market-leading capsule endoscope, i.e. 11 mm in diameter and 26 mm in length [10]. Researchers have developed different propulsion methods, and among many of them, the self-propelled system driven by autogenous interactive forces using magnetic actuation is a promising solution with growing interests in recent years, see e.g. [11–14]. The driving principle of these systems is illustrated in Fig. 1, where the rectilinear motion of the capsule system can be obtained through overcoming external resistance described as dry friction using a periodically driven internal mass interacting with the main body of the system. The advantage of this method is that no external moving components, such as clampers or fins, are required, so the system can be encapsulated and move independently in a complex environment. In order to validate this concept, an experimental investigation of a mesoscale prototype of the vibro-impact self-propelled capsule system, which is 19.4 mm in diameter and 56.9 mm in length, moving in a synthetic small intestine is presented in this paper. We will study the dynamics of the prototype, verify its modelling approach [15], and optimise the system in terms of its average progression velocity, power consumption and energy efficiency.

Vibro-impact driven machines are very popular in the past decade which have been used in many engineering applications, such as impact-forming machine [18], ground moling [19–21], vibro-impact drilling [22–25], energy harvesting [26], and pipeline robots [27,28]. The performance of these machines could be enhanced when their vibrational impacting motion is excited in resonance. For example, the best progression rate can be achieved by the high-frequency vibro-impact drilling [23] when its response is periodic, and its resonant condition may change once the drilled formation varies [24]. The effect of inertial mass and excitation frequency of a vibro-impact drifting system was investigated by Nguyen *et al.* [29] numerically and experimentally. Both forward and backward motion of the system was observed at some range of its mass ratio and excitation frequency. In [30], a new bidirectional drifting system with two-sided impacts excited by a periodic pulsed force was studied, and the direction of the system can be controlled by changing the direction of the excitation force. A challenging problem for these vibro-impact systems is the control of their complex dynamics, particularly when grazing events are encountered. Pavlovskaia et al. [31] studied the very rich dynamics of a one-degree-of-freedom oscillating system with one-sided impact close to grazing. It was found that the evolution of its attractor was governed by a complex interplay between smooth and nonsmooth bifurcations, and the interactions among a number of coexisting orbits. Rich coexisting attractors were also observed in a two-degrees-of-freedom vibro-impact capsule system [32] when it was operated in a complex frictional environment. Understanding of near-
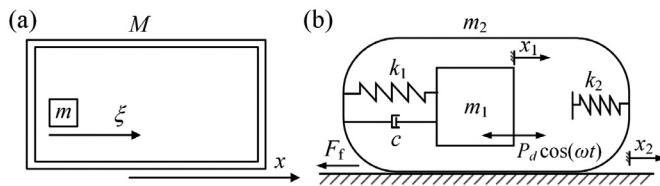

Fig. 1. (a) The two-mass system (adopted from [16]), and (b) the vibro-impact self-propelled capsule system (adopted from [17]).

grazing dynamics of vibro-impact systems is tricky, and special mathematical tools are required to gain an insight into this question. Jiang and Wiercigroch [33] extended the concept of discontinuity geometry of rigid impact oscillators to a soft impact oscillator. Jiang et al. [34] studied grazing bifurcations of a rigid and a soft impact oscillators by using a path-following method. Shan et al. [35] developed a high order discontinuity mapping for analysing the near-grazing dynamics of a multi-degrees-of-freedom impact oscillator. However, in the present work, our focus is not on the complex dynamics of the prototype close to grazing, but on the feasibility study of the vibro-impact propulsion technique under different frictional environments. Therefore, both our experiments and numerical simulations were carried out in the parametric regime at which such a complexity was minimised. For a detailed bifurcation analysis of the prototype, interested readers can refer to [36].

In recent years, vibro-impact driven robots have attracted great attention from the robotics community, see e.g. [37]. For example, Ivanov [38] studied an impact-driven capsule robot with a special design of its forcing profile in order to gain a desired progression. Nunuparov et al. [39] developed a capsule robot with an opposing spring driven by a periodic pulse-width force acting between the housing and its internal body. In [12], Nagy et al. numerically studied the motion of a complex micro-robot exhibiting impact and friction and compared with experimental observation. They found that the stiction and sliding of the robot were governed by excitation frequency and environmental friction, while impacts around the resonant frequency of the robot did not contribute to its propulsion. In this paper, we will consider three nonsmooth nonlinearities in our capsule system, i.e. friction, impact and square wave excitation, both numerically and experimentally, and investigate the dynamical responses of this system under variations of different control parameters (e.g. the frequency, amplitude and duty cycle ratio of the square wave excitation) and environmental resistances. One of the notable differences between the micro-robot studied in [12] and the capsule system studied in this paper is that, the former is operated in kilohertz and direct observation of the nonsmooth phenomena, such as impact and stick-slip motion, at microscale is difficult, while the latter is controlled at a much lower frequency (≤ 20 Hz), so the vibro-impact dynamics of the system can be easily studied. Hence, after an appropriate rescaling through nondimensionalisation (e.g. [17]), the findings of this paper could provide a better insight for this kind of robots under high frequency excitation, and the mesoscale prototype used in this paper can be used to predict the dynamical responses of these robots.

One major obstacle of current capsule robots is their limited on-board power for propulsion which restricts their efficiencies in motion control. The driving force provided by the miniature actuator is insufficient to overcome the resistance in the small intestine. If the driving force is increased, the limited on-board power cannot last for long operation. Therefore, a power utilisation strategy is vital for prototype development and optimisation. In [13], a multi-coil inductive powering system was designed for a vibratory driven capsule robot to address the power shortage issue, and a frictional reduction approach by using a rotational vibratory motor for this robot was studied in [14]. Since only partial power contributes to the progression of the robot, rotational vibration is not an efficient way of driving. In [40], a capsule robot driven by a linear vibratory actuator was designed, and its frictional resistance in the small intestine was studied [41,42]. In order to enhance its pro-

gression, we introduce two-sided constraints for the linear vibratory actuator which can generate notable impacts for capsule progression. By utilising the resonance of the forward and backward constraints, our capsule could achieve its maximal forward and backward progression speeds, respectively.

In [17], the dynamics of a vibro-impact capsule system with one-sided constraint under harmonic excitation was studied numerically by using the modelling approach for nonsmooth dynamical systems. It was found that the control parameters of the system for obtaining the best progression and the minimum power consumption are different, and therefore, a trade-off between these performance indices is required. An experimental verification of the vibro-impact capsule model was presented in [43] which shows a good agreement with the numerical results studied in [17] for a broad range of control parameters. The conducted bifurcation analysis indicates that the behaviour of the system is mainly periodic and that a fine tuning of the control parameters, e.g. the stiffness of the constraint, the frequency and amplitude of excitation, can significantly improve system's performance. In this paper, we will study the performance of the vibro-impact capsule system with two-sided constraints under the excitation of square wave numerically and experimentally. In addition to the findings in [17,43], the proposed vibro-impact mechanism can give us more flexibility in the motion control of the capsule, and the study in this paper will validate this concept in a more realistic environment, so provide a forward step towards prototype miniaturisation.

The rest of the paper is organised as follows. In Section 2, experimental setup of the capsule system is presented. In Section 3, the mathematical model of the vibro-impact capsule system described using nonsmooth multibody dynamics is introduced. Numerical simulations using the proposed mathematical model are then compared with experimental results in Section 4. Finally, some conclusions are drawn in Section 5.

2. Experimental apparatus

2.1. Prototype

The mesoscale prototype of the capsule system is shown in Fig. 2, which is 19.4 mm in diameter and 56.9 mm in length. A solenoid was mounted inside the capsule with its coil fixed to the inner surface of the capsule and a shaft acting as the inner mass. The shaft was connected to the coil by a helical spring at one end, and on the other end of the shaft, a nylon nut and an iron washer were fixed. When the coil was switched on, the shaft moved forward and compressed the helical spring. Forward impacts occurred when the washer hit the forward constraint. When the coil was switched off and the shaft returned back forced by the compressed spring. Backward impacts occurred when the nut hit the coil. The capsule might move forward or backward when the interaction force between the capsule and the shaft exceeded the environmental resistance. An accelerometer, 8640A50 manufactured by Kistler, and a linear variable differential transformer (LVDT), AML/EU10+/-200mm-C0R-02-000 manufactured by Applied Measurements, were used to measure the acceleration of the shaft and the displacement of the capsule, respectively. The accelerometer was of high sensitivity to its acceleration, but of low sensitivity to its base strain. To minimise the effect of the impact force on the accelerometer, a ground isolated adhesive mounting base, 800M158 manufactured by Kistler, the black cuboid shown in Fig. 2(c), was used to connect the accelerometer with the shaft. In addition, the measurement range of the accelerometer was ± 50 g with overload protection.

2.2. Experimental setup

The schematics of the experimental set-up is shown in Fig. 3. A solenoid was controlled by a self-assembled drive circuit, triggered by a pulse-width modulation (PWM) signal generated from a signal generator (AFG-2105 manufactured by GW Instek). The acceleration of the
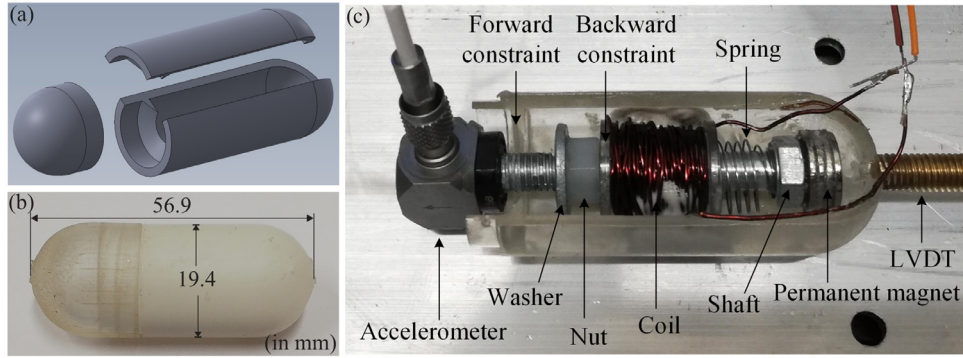
Fig. 2. (a) Exploded, (b) external and (c) internal views of the mesoscale capsule prototype [36]. A solenoid was mounted inside the capsule with its coil fixed to the inner surface of the capsule. The shaft of the solenoid connected with a washer via a nut, and the washer impacted with the forward and backward constraints when an excitation force was generated by the coil. A permanent magnet was attached at the end of the shaft to enhance the excitation force, and a helical spring was used to provide restoring force for the shaft. An accelerometer and a linear variable differential transformer were used to measure the acceleration of the shaft and the displacement of the capsule, respectively.
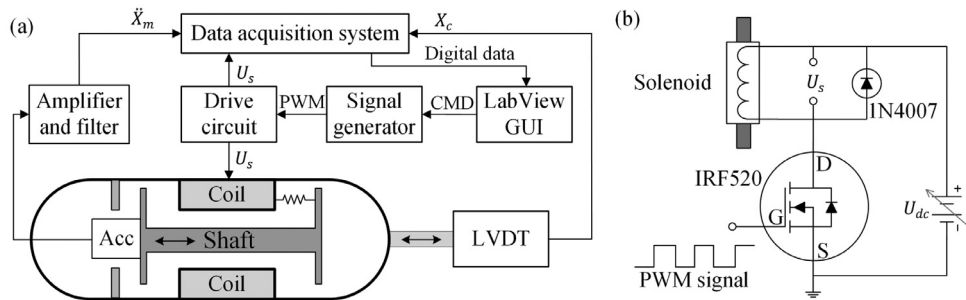

Fig. 3. (a) Schematics of the experimental setup and (b) the drive circuit of the solenoid. The solenoid was controlled by a drive circuit triggered by a pulse-width modulation signal generated from a signal generator. The acceleration of the shaft, the displacement of the capsule, and the voltage of the solenoid were recorded by a National Instruments data acquisition card, and a graphic user interface (GUI) coded in LabView. A power MOSFET transistor, IRF520NPBF, was used to provide switching-on and -off actions for the solenoid based on the pulse-width modulation (PWM) signal. This transistor could only control the frequency and duty cycle ratio of the voltage across the solenoid, while the amplitude of the solenoid voltage was controlled manually by adjusting the changeable DC power supply.

shaft, the displacement of the capsule, and the voltage of the solenoid were recorded by a National Instruments data acquisition (DAQ) card, USB6210, and a graphic user interface (GUI) coded in LabView. The sampling rate of the DAQ card was configured at 1 kHz, and the GUI sent commands (CMDs) to the signal generator to vary the frequency and duty cycle ratio of the PWM signal. Fig. 3(b) details the drive circuit. A changeable DC power supply, 72-10495 manufactured by TENMA, was applied to power up the actuator. A power MOSFET transistor, IRF520NPBF manufactured by Infineon Technologies, was used to provide switching-on and -off actions based on the PWM signal. This transistor could only control the frequency and duty cycle ratio of the voltage across the solenoid, and the amplitude of the solenoid voltage was controlled manually by adjusting the changeable DC power supply.

In order to investigate capsule's dynamics under various friction environments, three contact cases as shown in Fig. 4 are considered in this study, which are

- Case 1: the capsule moves on an aluminium bench;
- Case 2: the capsule moves on a cut-open synthetic small intestine;
- Case 3: the capsule moves in a complete synthetic small intestine being held by a polyvinyl chloride tube.

It should be noted that since the accelerometer cannot fit into the tube, only the displacement of the capsule was measured for Case 3.

2.3. Data processing

Since the progression velocity and the energy efficiency of the prototype are the main performance indices to be evaluated, after each experimental run, a segment of measured data was used to calculate the
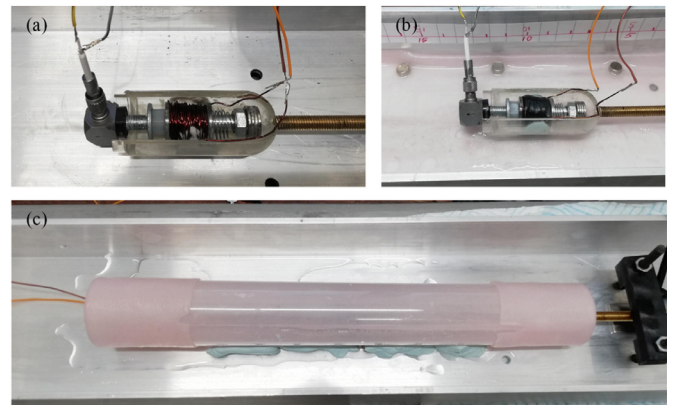

Fig. 4. Photographs of the prototype moving on (a) Case 1: an aluminium bench, (b) Case 2: a cut-open synthetic small intestine, and in (c) Case 3: a complete synthetic small intestine being held by a polyvinyl chloride tube.

average progression velocity of the capsule and the average power consumption of the solenoid for the time interval, $t \in [N_0 T, N_0 T + N_a T]$, where T is the excitation period, and N_0 and N_a are the period numbers. Here, the average progression velocity of the capsule, V_{avg}, was calculated as

$$V_{avg} = \frac{X_l(N_0 T + N_a T) - X_l(N_0 T)}{N_a T}, \tag{1}$$

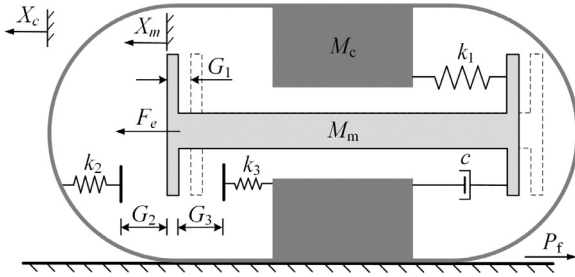where $X_l(t)$ represents LVDT's measurement.

Fig. 5. Schematic diagram of the capsule prototype.

The voltage of the solenoid, U_s, was recorded by the DAQ system, and the excitation force, F_{exp}, was calculated as

$$F_{exp} = k_i I_s = k_i \frac{U_s}{R_s}, \tag{2}$$

where k_i, I_s and R_s are the force-current ratio, the current and the resistance of the solenoid, respectively. Then the average power consumption of the solenoid, P_{avg}, was computed as

$$P_{avg} = \frac{1}{N_a T} \int_{N_0 T}^{N_0 T + N_a T} \frac{U_s^2}{R_s}. \tag{3}$$

Therefore, the average energy efficiency of the prototype, E_{avg}, was obtained as

$$E_{avg} = V_{avg}/P_{avg}. \tag{4}$$

3. Mathematical modelling and parameter identification

3.1. Equations of motion

Mathematical model of the capsule prototype is presented in Fig. 5, where k_1 represents the stiffness of the physical spring connecting the shaft and the capsule, and c is the damping coefficient representing the energy dissipation led by the relative velocity between the capsule and the shaft. The forward constraint is modelled as a secondary spring with stiffness k_2, and the backward constraint is modelled as a tertiary spring with stiffness k_3, providing forward and backward impacts, respectively. The pre-compressed distance of the physical spring is defined as G_1. The gap between the shaft and the forward constraint is G_2, and G_3 represents the gap between the shaft and the backward constraint. M_c and M_m are the masses of the capsule (including the mass of the LVDT rod) and the shaft (including the mass of the accelerometer), respectively. X_c is the displacement of the capsule, and X_m is the displacement of the shaft. The friction between the capsule and its supporting surface is modelled as the Coulomb friction with the friction coefficient μ for all the three cases.

It can be seen from Fig. 5 that three nonsmooth nonlinearities are involved in the model, which are the PWM excitation, impact and friction. The PWM excitation, F_e, is a switch-on and -off signal which can be expressed as

$$F_e(t) = \begin{cases} P_d, & t \in [NT, NT + DT], \\ 0, & t \in (NT + DT, NT + T), \end{cases} \tag{5}$$

where N is the period number, P_d, $f = \frac{1}{T}$ and $D \in (0, 1)$ are the amplitude, frequency and duty cycle ratio of the PWM excitation, respectively.

Next, we define the interaction force acting on the inner mass (shaft) M_m as F_i, written as

$$F_i = \begin{cases} F_e - F_1 - cV_r - F_3, & X_r \leq -G_3, \\ F_e - F_1 - cV_r, & -G_3 \leq X_r \leq G_2, \\ F_e - F_1 - cV_r - F_2, & X_r \geq G_2, \end{cases} \tag{6}$$

where $X_r = X_m - X_c$ and $V_r = V_m - V_c$ represent the relative displacement and velocity between the inner mass and the capsule, respectively.

Table 1
Identified parameters of the capsule prototype.

Parameters	Unit	Case 1	Case 2	Case 3
k_i	mN/A	55	55	55
R_s	Ω	0.72	0.72	0.72
M_c	g	82.42	82.42	86.26
M_m	g	15.2	15.2	9.77
μ	–	0.3117	0.2771	0.2293
G_1	mm	0	0	0
G_2	mm	3.4	3.4	3.4
G_3	mm	0	0	0
k_1	kN/m	0.04	0.052	0.07
k_2	kN/m	16.35	20.91	28
k_3	kN/m	12.27	15.68	21
c	Ns/m	0.53	0.87	0.99

$F_1 = k_1(X_r + G_1)$, $F_2 = k_2(X_r - G_2)$, and $F_3 = k_3(X_r + G_3)$ represent the interaction forces for the physical spring, forward and backward impacts, respectively. Since the contacting surfaces for both the aluminium and the small intestine were smooth and the instant speed of the capsule was fast in experiments, the capsule dynamics due to low speed and the Stribeck effect are neglected, and only the Coulomb friction is considered in the model. So,

$$F_f = \begin{cases} -\text{sign}(V_c)P_f, & V_c \neq 0, \\ \text{sign}(F_i)P_f, & V_c = 0, |F_i| \geq P_f, \\ F_i, & V_c = 0, |F_i| \leq P_f, \end{cases} \tag{7}$$

where $P_f = \mu(M_m + M_c)g$ is the static friction of the prototype, and g is the gravitational acceleration.

Finally, the equations of motion of the capsule prototype can be written as

$$\begin{cases} M_m \ddot{X}_m = F_i, \\ M_c \ddot{X}_c = -F_i + F_f. \end{cases} \tag{8}$$

3.2. Parameter identification

The total weight of the shaft and the accelerometer provides the value of the inner mass M_m, while the weight of the remaining parts, including the coil, the capsule shell and LVDT's rod, gives the mass of the capsule M_c. They were simply measured by weighting each element and kept constant throughout the experiments. The coefficients, k_1, k_2, k_3 and c, were identified by matching numerical simulation with each experimental run, and then averaged for all experimental runs. Identification of friction coefficient μ between the capsule and the supporting surface was carried out by lifting one side of the supporting surface slowly until the stationary capsule started to move. So, the friction coefficient was determined by the angle of the surface slope at that moment. Finally, the identified physical parameters of the capsule prototype are given in Table 1.

4. Experimental and numerical results

In this section, experimental and numerical results are compared. Our numerical simulations were carried out by using the first-order Euler method with a fixed time step of $1/10^4$ of the excitation period, as the Euler method can balance the computational accuracy and cost effectively. A condition loop was implemented in the algorithm by monitoring the relative displacement and the gap between the shaft and the capsule to switch between impact and non-impact cases.

4.1. Case 1: aluminium bench

Experimental and numerical results of average progression velocity of the capsule prototype by varying the frequency, amplitude and duty cycle ratio of the PWM excitation for Case 1 when the prototype moves
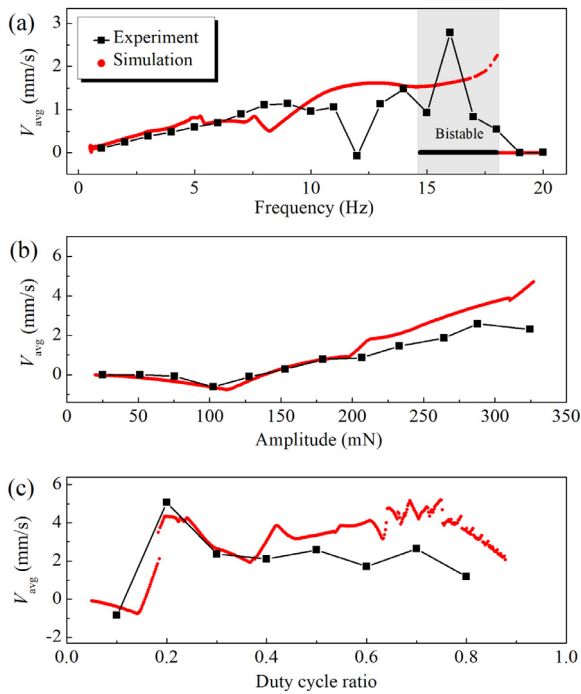
Fig. 6. Experimental and numerical average velocities of the capsule for Case 1 (aluminium bench) under the conditions of (a) $P_d = 183.3$ mN, $D = 0.5$ and $f \in [0.5, 20]$ Hz, (b) $f = 9$ Hz, $D = 0.5$ and $P_d \in [20, 340]$ mN, and (c) $P_d = 282.6$ mN, $f = 9$ Hz and $D \in [0.05, 0.95]$. Grey shadowed area indicates the bistability of the prototype at where two stable motions (red dots: forward progression and black dots: sticking) coexist.

on an aluminium bench are presented in Fig. 6. As can be seen from the figure, the numerical results show a good agreement with the experimental results under a wide range of excitation parameters. It can be observed from Fig. 6(a) that, the capsule has faster forward progression for the frequency range $f \in [14.5, 18]$ Hz. When the amplitude of excitation increases as shown in Fig. 6(b), the average velocity decreases to -0.76 mm/s for $P_d = 102.4$ mN initially, which indicates a backward progression of the capsule. As the amplitude increases further, the average velocity of the capsule increases to 5.29 mm/s. When the duty cycle

ratio increases, the average progression velocity varies from -0.85 mm/s to 5.21 mm/s as shown in Fig. 6(c) at where the maximum velocity is achieved at $D = 0.2$.

Two examples of time histories of capsule's responses are presented in Fig. 7. In Fig. 7(a), it can be observed that, only backward impacts between the shaft and the capsule occur, which lead to a backward progression of the capsule. In Fig. 7(b), both forward and backward impacts are encountered, but the forward impacts are much stronger than the backward ones, so the capsule has a forward progression overall.

Multistability has been observed in the capsule prototype which is shown in the grey shadowed area of Fig. 6(a), where the system has a period-1 forward motion coexisting with a period-1 motion with no progression. We took a further investigation at this bistability by numerically plotting the basins of attraction of the capsule prototype for $f = 16$ Hz in Fig. 8. As can be seen from the figure, green and blue areas represent all the initial conditions of the prototype that converge to the period-1 forward motion and the period-1 stationary motion, respectively. As the prototype may have two responsive modes in this bistable region, the position feedback controller studied in [32] can be used to suppress this phenomenon.

4.2. Case 2: cut-open small intestine

For Case 2 when the capsule moves on a cut-open small intestine, the comparison between experimental and numerical results is presented in Fig. 9. As can be seen from Fig. 9(a), the average velocity of progression increases as the excitation frequency increases when $f \in [0.5, 18]$ Hz, and then decreases when $f \in (18, 20]$ Hz, under the condition of $P_d = 290.3$ mN and $D = 0.5$. The maximum average velocities of forward and backward progression observed in experiments are 6.66 mm/s and -0.06 mm/s, respectively. Fig. 9(b) shows how the excitation amplitude influences the performance of the capsule under the condition of $f = 18.5$ Hz, $D = 0.5$ and $P_d \in [20, 340]$ mN. It can be seen that there exists an amplitude threshold for moving the capsule, which is about $P_d = 213.9$ mN in experiment, and $P_d = 261.1$ mN in numerical simulation. In Fig. 9(c), it shows how the duty cycle ratio influences the capsule under the condition of $P_d = 275.8$ mN, $f = 18.5$ Hz and $D \in [0.05, 0.95]$. There are some differences between the experimental and numerical average velocities when $D > 0.3$, but their trends are the same.

An interesting bifurcation phenomenon observed in experiments is shown in Fig. 10, where the motion of the prototype changes from period-1 backward motion to period-2 forward motion, and then to
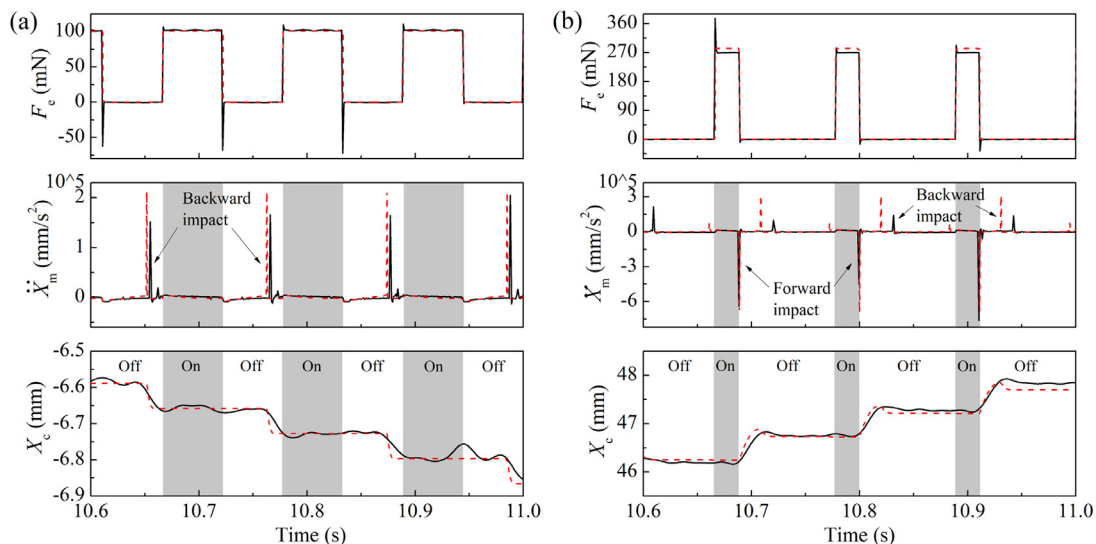

Fig. 7. Experimental (black solid lines) and numerical (red dashed lines) time histories of the excitation force (upper panel), the inner mass acceleration (middle panel) and the capsule displacement (lower panel) for (a) $f = 9$ Hz, $P_d = 100.8$ mN, and $D = 0.5$, and (b) $f = 9$ Hz, $P_d = 282.6$ mN, and $D = 0.2$.
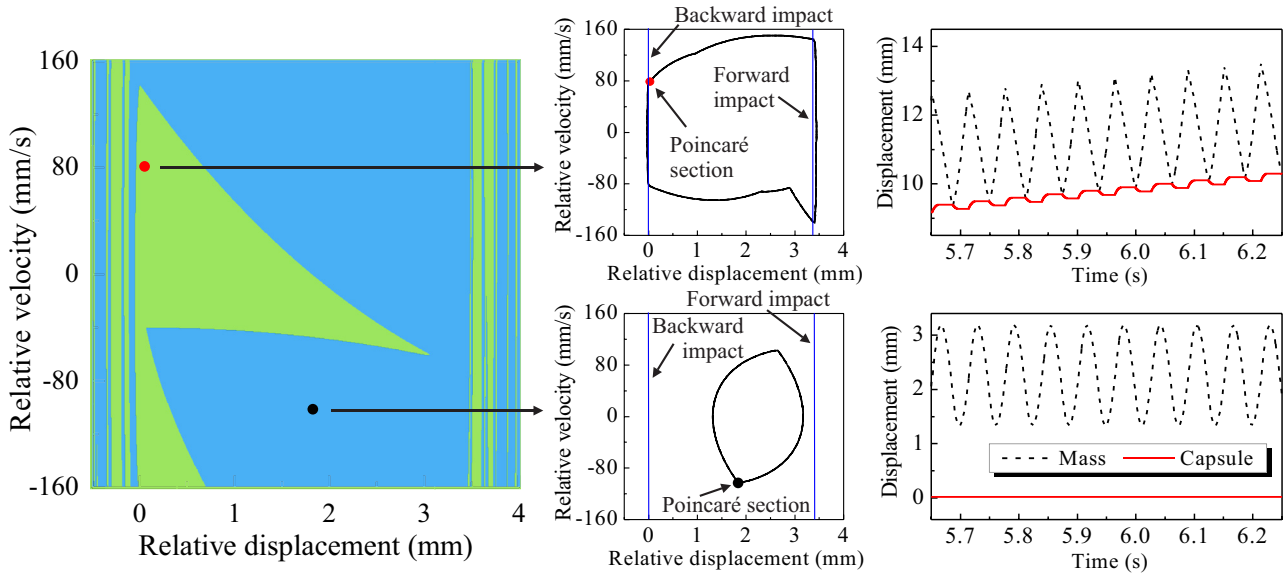
Fig. 8. Basins of attraction of the bistable (grey shadowed) area shown in Fig. 6, where $P_d = 183.3$ mN, $D = 0.5$ and $f = 16$ Hz. Red dot with green basin represents the period-1 forward motion with forward and backward impacts, and black dot with blue basin represents the period-1 stationary motion with no impact. Blue lines shown in the phase portraits represent the forward and backward impact boundaries.
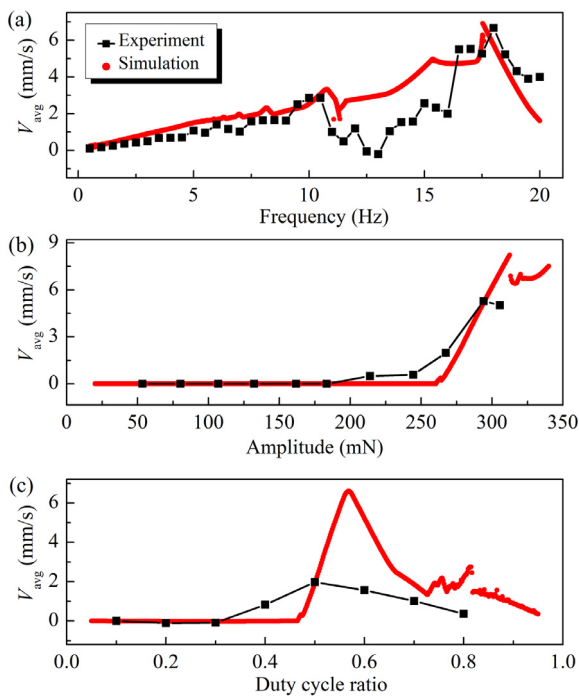

Fig. 9. Experimental and numerical average velocities of the capsule for Case 2 (cut-open small intestine) under the conditions of (a) $P_d = 290.3$ mN, $D = 0.5$ and $f \in [0.5, 20]$ Hz, (b) $f = 18.5$ Hz, $D = 0.5$ and $P_d \in [20, 340]$ mN, and (c) $P_d = 275.8$ mN, $f = 18.5$ Hz and $D \in [0.05, 0.95]$.

Fig. 10. Experimental time histories of the shaft acceleration (red lines) and the capsule displacement (blue lines) for Case 2 (cut-open small intestine) recorded for $P_d = 275.8$ mN, $f = 18.5$ Hz, $D = 0.3$ (upper panel), $D = 0.4$ (middle panel) and $D = 0.5$ (lower panel). It can be observed that the prototype bifurcates from a period-1 backward motion to a period-2 forward motion, and then to a period-1 forward motion when the duty cycle ratio increases.

period-1 forward motion when the duty cycle ratio increases from 0.3 to 0.5. As can be seen from the figure, when $D = 0.3$, there is no impact, so the capsule has very slow backward progression. When $D = 0.4$, forward impacts emerge and the capsule starts to move forward. However, one forward impact happens in every two periods, so the forward progression of the capsule is slow. Once $D = 0.5$, the response of the capsule bifurcates from period-2 into period-1 motion with one impact per period of excitation. Therefore, the forward progression of the capsule becomes faster.
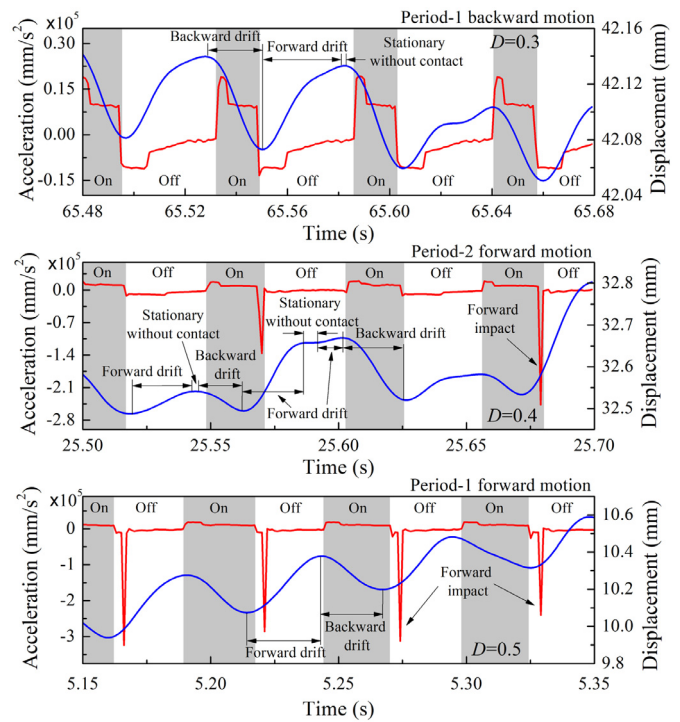
4.3. Case 3: complete small intestine

Experimental and numerical results for Case 3 when the prototype moves in a complete small intestine are presented in Fig. 11. As shown in Fig. 11(a), the average progression velocity of the capsule varies from -0.01 mm/s to 2.32 mm/s under the condition of $P_d = 282.6$ mN, $D = 0.5$
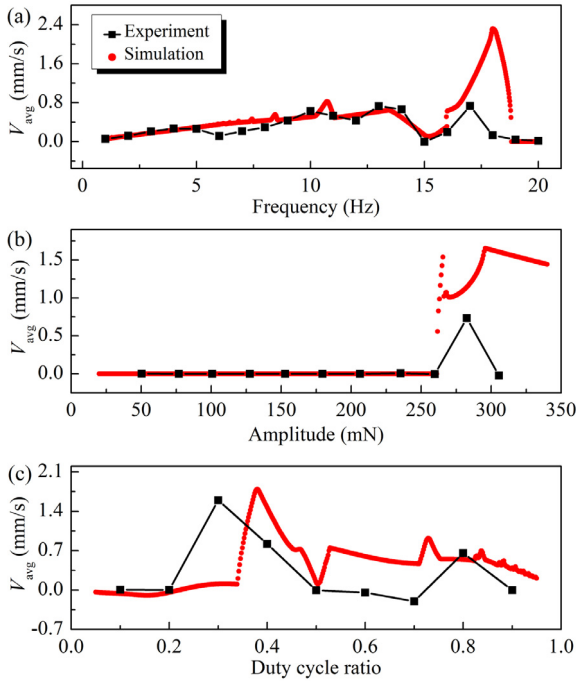
Fig. 11. Experimental and numerical average velocities of the capsule for Case 3 (complete small intestine) under the conditions of (a) $P_d = 282.6$ mN, $D = 0.5$ and $f \in [0.5, 20]$ Hz, (b) $f = 17$ Hz, $D = 0.5$ and $P_d \in [20, 340]$ mN, and (c) $P_d = 282.6$ mN, $f = 15$ Hz and $D \in [0.05, 0.95]$.

and $f \in [0.5, 20]$ Hz. In Fig. 11(b), we can observe that the threshold amplitude is about 282.6 mN under the condition of $f = 17$ Hz, $D = 0.5$ and $P_d \in [20, 340]$ mN. By varying the duty cycle ratio as shown in Fig. 11(c), the average progression velocity of the capsule can vary from -0.01 mm/s to 1.60 mm/s under the condition of $P_d = 282.6$ mN, $f = 15$ Hz and $D \in [0.05, 0.95]$.

Due to the size of the accelerometer which cannot fit into the complete small intestine, acceleration of the inner mass for Case 3 was not measured and only the displacement of the prototype was recorded. However, we can estimate the dynamics of the capsule from Case 1 when the prototype has similar parameter configurations. An example of this investigation is presented in Fig. 12, where the experimental result of Case 1 is compared with the one of Case 3. It can be inferred from the figure that the prototype in Case 3 has both forward and backward impacts. Since the prototype in Case 1 has larger friction, there are intervals within which the capsule is stationary, and this helps the capsule to retain its position for a more efficient forward progression. For Case 3, friction is smaller, and such a stationary interval does not exist, so the prototype has forward and backward drifts only, leading to a slow and inefficient forward progression.

4.4. Energy efficiency and optimisation

Experimental energy efficiencies calculated using Eq. (4) for these three cases are presented in Fig. 13. As we can see from the figure, the energy efficiencies for these three cases have similar trends under the variations of excitation frequency, amplitude and duty cycle ratio. The prototype has better efficiency when it moves on the aluminium bench and the cut-open small intestine, and becomes bad when it moves in the complete small intestine. Based on these experimental data, the best operational control parameters for forward progression are $f \in [15, 20]$ Hz, $P_d \in [250, 300]$ mN and $D \in [0.2, 0.5]$.
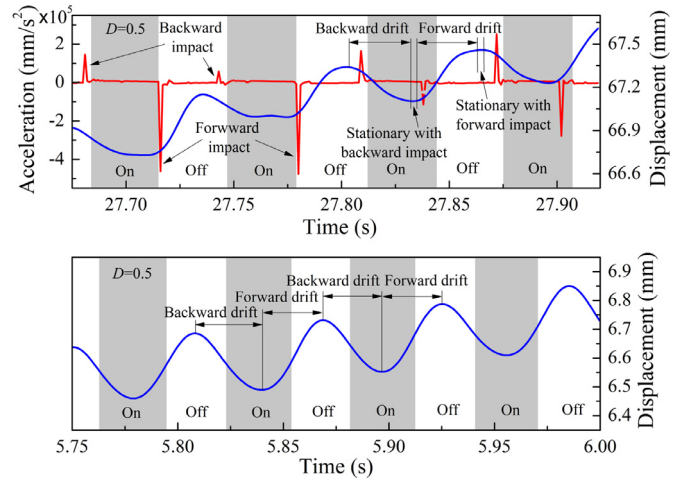

Fig. 12. Experimental time histories of shaft acceleration (red) and capsule displacement (blue) recorded for (upper panel) Case 1: $f = 16$ Hz, $P_d = 183.3$ mN, and $D = 0.5$ on the aluminium bench and (lower panel) Case 3: $f = 17$ Hz, $P_d = 282.6$ mN, and $D = 0.5$ in the complete small intestine.
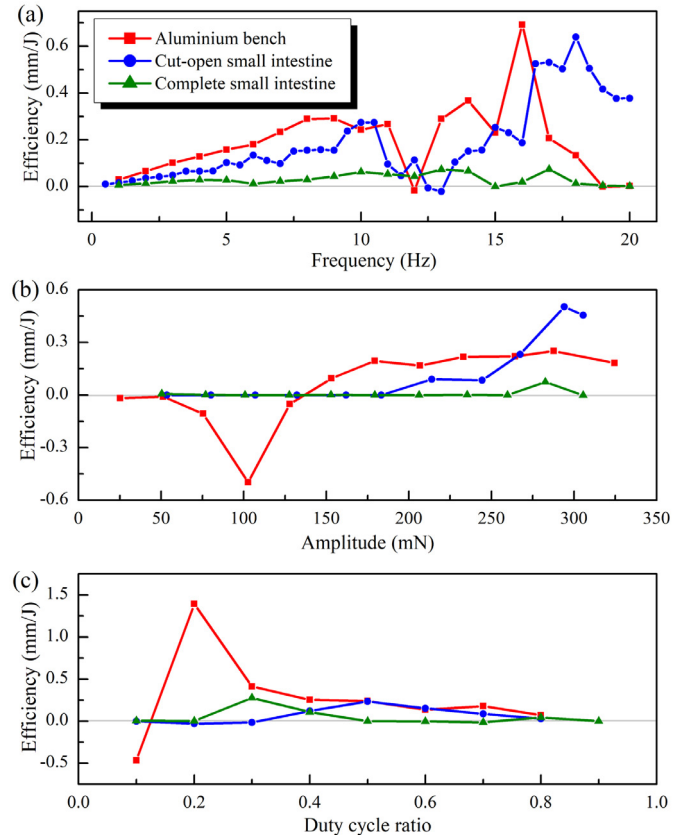

Fig. 13. Energy efficiencies of the prototype under variations of (a) excitation frequency, (b) excitation amplitude and (c) duty cycle ratio. Red squares, blue circles and green triangles represent the experiments carried out on the aluminium bench (Case 1), on the cut-open small intestine (Case 2) and in the complete small intestine (Case 3).

Although the dimension of the mesoscale prototype studied in this paper is much larger than the dimension of the standard-sized capsule endoscope [10] (11 mm in diameter and 26 mm in length), our numerical simulations fit well with the experimental data, so validate the efficacy of the proposed mathematical model in Eq. (8). Hence, if we scale down the capsule size to the standard one, our
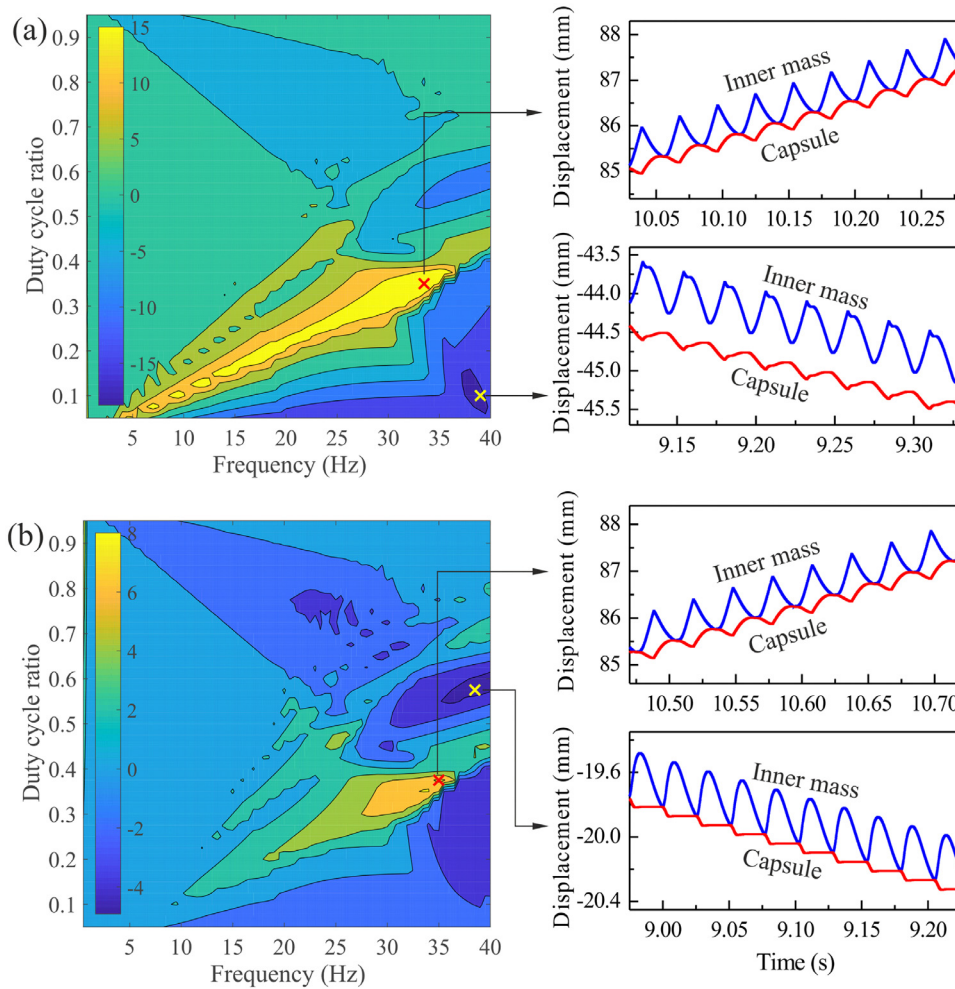
Fig. 14. Numerical predictions of (a) energy efficiencies and (b) average progression velocities at the amplitude of excitation $P_d = 70$ mN under variations of excitation frequency and duty cycle ratio when the capsule moves in a complete small intestine. Red and yellow crosses represent (a) the most efficient forward progression (at $f = 33.5$ Hz and $D = 0.35$) and the most efficient backward progression (at $f = 39$ Hz and $D = 0.1$), and (b) the fastest forward (at $f = 35$ Hz and $D = 0.375$) and backward (at $f = 38.5$ Hz and $D = 0.575$) progressions, respectively.

Table 2
Anticipated parameters for the standard-sized prototype.

Parameters	Value	Unit
M_c	6	g
M_m	2.12	g
μ	0.2293	–
G_1	0	mm
G_2	1	mm
G_3	0	mm
k_1	0.047	kN/m
k_2	18.8	kN/m
k_3	14.1	kN/m
c	0.33	Ns/m
P_d	70	mN

proposed model in Eq. (8) can be used to predict the performance of the self-propelled capsule in standard dimension. Next, we assume that a cylindrical iron shaft with 6 mm in diameter and 10 mm in length is installed in the capsule for actuation, so the shaft weights about $M_m = 2.12$ g. The winding coil may weight around 2 g approximately, and the capsule shell is about 4 g in weight, so $M_c = 6$ g for the scaled-down capsule prototype. Finally, the rest of the anticipated parameters for the standard-sized prototype are summarised in Table 2.

Based on the anticipated parameters of the scale-down capsule prototype, numerical predictions for Case 3 under the variations of excitation frequency and duty cycle ratio calculated by using the mathemat-

ical model in Eq. (8) are presented in Fig. 14. As shown in Fig. 14(a), the best energy efficiency for forward progression is 19.78 mm/J when $f = 33.5$ Hz and $D = 0.35$, and the best energy efficiency of backward progression is −18.74 mm/J when $f = 39$ Hz and $D = 0.1$. In Fig. 14(b), the fastest forward progression is recorded for $f = 35$ Hz and $D = 0.375$ producing an average velocity of 8.49 mm/s, and the fastest backward progression is found at $f = 38.5$ Hz and $D = 0.575$ generating an average velocity of −4.9 mm/s.

5. Conclusions

This paper carried out an experimental investigation by using a mesoscale prototype for proof-of-concept of the self-propelled capsule endoscopy for small-bowel examination. A new mathematical model of the prototype was developed to study the dynamical characteristics of the system. The performance of the prototype was investigated both experimentally and numerically in terms of average progression velocity and energy efficiency, under variations of excitation frequency, amplitude and duty cycle ratio. Three different frictional scenarios, i.e. moving on an aluminium bench, on a cut-open small intestine and in a complete small intestine, were tested to demonstrate the efficacy of the proposed self-propulsion technique.

Our analysis shows that the environmental resistance between the capsule and the small intestine plays an important role in capsule's locomotion. In order to maintain capsule's efficiency, friction should be appropriate, and lower friction could cause capsule oscillate at its original position so degrading its performance. Based on our optimisation for the standard-sized capsule prototype, the maximum average velocity

for forward progression is up to 8.49 mm/s, indicating that the capsule can travel through a 6 m long small intestine in 12 min, offering the potential for a 'live' and controllable examination.

Our future work will focus on prototype design and optimisation of the standard-sized capsule, closed-loop control system design for capsule's locomotion, and *ex vivo* test.

Data accessibility

The datasets generated and analysed during the current study are available from the corresponding author on reasonable request.

Declaration of Competing Interest

The authors declare that they have no conflict of interest concerning the publication of this manuscript.

The authors declare that they have no known competing financial interests or personal relationships that could have appeared to influence the work reported in this paper.

CRediT authorship contribution statement

Bingyong Guo: Methodology, Software, Validation, Formal analysis, Investigation, Writing - original draft, Visualization. **Yang Liu:** Conceptualization, Methodology, Writing - review & editing, Visualization, Supervision, Funding acquisition. **Rauf Birler:** Validation, Investigation. **Shyam Prasad:** Conceptualization, Methodology, Supervision.

Acknowledgments

References

[1] Simi M, Valdastri P, Quaglia C, Menciassi A, Dario P. Design, fabrication and testing of a capsule with hybrid locomotion for gastrointestinal tract exploration. IEEE-ASME T Mech 2010;15:170–80.

[2] Zhang Y, Jiang S, Zhang X, Ruan X, Guo D. A variable-diameter capsule robot based on multiple wedge effects. IEEE-ASME T Mech 2011;16:241–54.

[3] Yim S, Sitti M. Design and rolling locomotion of a magnetically actuated soft capsule endoscope. IEEE T Robot 2012;28:183–94.

[4] Zhou H, Alici G, Than T, Li W. Modeling and experimental investigation of rotational resistance of a spiral-type robotic capsule inside a real intestine. IEEE-ASME T Mech 2013;18:1555–62.

[5] Liu L, Towfighian S, Hila A. A review of locomotion systems for capsule endoscopy. IEEE Rev Biomed Eng 2015;8:138–51.

[6] Gao J, Yan G, Wang Z, He S, Xu F, Jiang P, et al. Design and testing of a motor-based capsule robot powered by wireless power transmission. IEEE-ASME T Mech 2016;21:683–93.

[7] Munoz F, Alici G, Zhou H, Li W, Sitti M. Analysis and magnetic interaction in remotely controlled magnetic devices and its application to a capsule robot for drug delivery. IEEE-ASME T Mech 2018;23:298–310.

[8] Glass P, Cheung E, Sitti M. A legged anchoring mechanism for capsule endoscopes using micropatterned adhesives. IEEE T Biomed Eng 2008;5:2759–67.

[9] Quirini M, Menciassi A, Scapellato S, Stefanini C, Dario P. Design and fabrication of a motor legged capsule for the active exploration of the gastrointestinal tract. IEEE-ASME T Mech 2008;13:169–79.

[10] Medtronic. *PillCam^tm SB 3 System*. Available at http://www.medtronic.com/covidien/en-us/products/capsule-endoscopy/pillcam-sb-3-system.html (31/12/18).

[11] Nelson B, Kaliakatsos I, Abbott J. Microrobots for minimally invasive medicine. Annu Rev Biomed Eng 2010;12:55–85.

[12] Nagy Z, Leine R, Frutiger D, Glocker C, Nelson B. Modeling the motion of microrobots on surfaces using nonsmooth multibody dynamics. IEEE T Robot 2012;28:1058–68.

[13] Carta R, Sfakiotakis M, Pateromichelakis N, Thoné J, Tsakiris D, Puers R. A multi-coil inductive powering system for an endoscopic capsule with vibratory actuation. Sens Actuators A-Phys 2011;172:253–8.

[14] Sfakiotakis M, Pateromichelakis N, Tsakiris D. Vibration-induced frictional reduction in miniature intracorporeal robots. IEEE T Robot 2014;30:1210–21.

[15] Yan Y, Liu Y, Liao M. A comparative study of the vibro-impact capsule systems with one-sided and two-sided constraints. Nonlinear Dyn 2017;89:1063–87.

[16] Chernousko FL. The optimum rectilinear motion of a two-mass system. J Appl Maths Mechs 2002;66:1–7.

[17] Liu Y, Wiercigroch M, Pavlovskaia E, Yu H. Modeling of a vibro-impact capsule system. Int J Mech Sci 2013;66:2–11.

[18] Luo GW. Dynamics of an impact-forming machine. Int J Mech Sci 2006;48:1295–313.

[19] Nguyen VD, Woo KC. Nonlinear dynamic responses of new electro-vibroimpact system. J Sound Vib 2008;310:769–75.

[20] Ho JH, Nguyen VD, Woo KC. Nonlinear dynamics of a new electro-vibro-impact system. Nonlinear Dyn 2011;63:35–49.

[21] Nguyen VD, Nguyen HC, Ngo NK, La NT. A new design of horizontal electro-vibro-impact devices. J Comput Nonlinear Dyn 2017;12:61002.

[22] Aguiar RR, Weber HI. Mathematical modeling and experimental investigation of an embedded vibro-impact system. Nonlinear Dyn 2011;65:317–34.

[23] Pavlovskaia E, Hendry DC, Wiercigroch M. Modelling of high frequency vibro-impact drilling. Int J Mech Sci 2015;91:110–19.

[24] Liu Y, Páez Chávez J, Pavlovskaia E, Wiercigroch M. Analysis and control of the dynamical response of a higher order drifting oscillator. Proc R Soc A 2018;474:20170500.

[25] Liao M, Liu Y, Páez Chávez J, Chong ASE, Wiercigroch M. Dynamics of vibro-impact drilling with linear and nonlinear rock models. Int J Mech Sci 2018;146–147:200–10.

[26] Serdukova L, Kuske R, Yurchenko D. Stability and bifurcation analysis of the period-t motion of a vibroimpact energy harvester. Nonlinear Dyn 2019;98:1807–19.

[27] Yan Y, Liu Y, Páez Chávez J, Zonta F, Yusupov A. Proof-of-concept prototype development of the self-propelled capsule system for pipeline inspection. Meccanica 2018;53:1997–2012.

[28] Yan Y, Liu Y, Jiang H, Peng Z, Crawford A, Williamson J, et al. Optimization and experimental verification of the vibro-impact capsule system in fluid pipeline. P I Mech Eng C-J Mec 2019;233:880–94.

[29] Nguyen V, Duong T, Chu N, Ngo Q. The effect of inertial mass and excitation frequency on a duffing vibro-impact drifting system. Int J Mech Sci 2017;124-125:9–21.

[30] Duong T, Nguyen V, Nguyen H, Vu N, Ngo N, Nguyen V. A new design for bidirectional autogenous mobile systems with two-side drifting impact oscillator. Int J Mech Sci 2018;140:325–38.

[31] Pavlovskaia E, Ing J, Wiercigroch M, Banerjee S. Complex dynamics of bilinear oscillator close to grazing. Int J Bifurc Chaos 2010;20:3801–17.

[32] Liu Y, Páez Chávez J. Controlling multistability in a vibro-impact capsule system. Nonlinear Dyn 2017;88:1289–304.

[33] Jiang H, Wiercigroch M. Geometrical insight into non-smooth bifurcations of a soft impact oscillator. IMA J Appl Math 2016;81:662–78.

[34] Jiang H, Chong ASE, Ueda Y, Wiercigroch M. Grazing-induced bifurcations in impact oscillators with elastic and rigid constraints. Int J Mech Sci 2017;127:204–14.

[35] Shan Y, Ji J, Wen G. Complex near-grazing dynamics in impact oscillators. Int J Mech Sci 2019;156:106–22.

[36] Liu Y., Páez Chávez J., Guo B., Birler R. Bifurcation analysis of a vibro-impact experimental rig with two-sided constraint. Meccanica, Under review.

[37] Xu J, Fang H. Improving performance: recent progress on vibration-driven locomotion systems. Nonlinear Dyn 2019. doi:10.1007/s11071-019-04982-y.

[38] Ivanov AP. Analysis of an impact-driven capsule robot. Int J Non-Linear Mech 2020;119:103257.

[39] Nunuparov A, Becker F, Bolotnik N, Zeidis I, Zimmermann K. Dynamics and motion control of a capsule robot with an opposing spring. Arch Appl Mech 2019;89:2193–208.

[40] Li H, Furuta K, Chernousko FL. Motion generation of the capsubot using internal force and static friction. In: Proceedings of the 45th IEEE Conference on Decision and Control, San Diego, CA, USA; 2006. p. 6575–80.

[41] Zhang C, Liu H, Tan R, Li H. Modeling of velocity-dependent frictional resistance of a capsule robot inside an intestine. Tribol Lett 2012;47:295–301.

[42] Zhang C, Liu H, Li H. Modeling of frictional resistance of a capsule robot moving in the intestine at a constant velocity. Tribol Lett 2014;53:71–8.

[43] Liu Y, Pavlovskaia E, Wiercigroch M. Experimental verification of the vibro-impact capsule model. Nonlinear Dyn 2015;83:1029–41.